Low-frequency Raman response near the Ising-nematic quantum critical point: A memory-matrix approach

Xiaoyu Wang [1] and Erez Berg [2]

[1]*National High Magnetic Field Laboratory, Tallahassee, Florida 32310, USA*
[2]*Department of Condensed Matter Physics, Weizmann Institute of Science, Rehovot 76100, Israel*

Recent Raman scattering experiments have revealed a quasielastic peak in $FeSe_{1-x}S_x$ near an Ising-nematic quantum critical point (QCP) [Zhang *et al.*, PNAS **118**, 20 (2021)]. Notably, the peak occurs at subtemperature frequencies, and softens as T^α when temperature is decreased toward the QCP, with $\alpha > 1$. This temperature dependence is inconsistent with an impurity scattering scenario, and suggests that quantum critical fluctuations play an important role. In this work, we incorporate these effects in the framework of a memory matrix approach. The quasielastic peak is associated with the relaxation of an Ising-nematic deformation of the Fermi surface. We identify the dynamical scattering rate τ^{-1} of this deformation as the product of the quasielastic peak frequency Γ and the Ising-nematic thermodynamic susceptibility χ. Over a broad temperature regime, we find that $\tau^{-1}(T)$ exhibits a quasilinear dependence on temperature, in qualitative agreement with experiments. This behavior reflects a crossover from quantum critical scaling to a regime where the lifetime is governed by scattering from quasielastic thermal fluctuations. At frequencies larger than the temperature, we find that the Raman response is proportional to $\omega^{1/3}$, consistently with earlier theoretical predictions.

I. INTRODUCTION

Many unconventional superconductors, such as the iron-based superconductors and hole-doped cuprates, host an Ising-nematic phase where the discrete crystalline rotational symmetry (C_4) is spontaneously broken [1–6]. Upon doping or pressure, the nematic transition temperature is suppressed to zero, pointing to a putative Ising-nematic quantum critical point (QCP), where the nematic susceptibility diverges [7–9]. Interestingly, close to the QCP, novel non-Fermi liquid behaviors have been observed, while the critical temperatures for superconductivity are also often enhanced. These observations point to the crucial role played by the critical Ising-nematic fluctuations in such systems [10–22].

Due to the presence of gapless quasiparticles near the Fermi surface, the dynamical properties of the critical fluctuations are strongly modified compared to those of an insulator. In the quasistatic and long wavelength limit ($\omega \ll |v_F \mathbf{q}|$) the dynamics is governed by Landau damping, i.e., the decay of critical fluctuations into collective electron-hole excitations near the Fermi surface. The purely dynamical limit ($\omega \gg |v_F \mathbf{q}|$) is much less studied. Raman scattering experiments in $FeSe_{1-x}S_x$, which probe the dynamics in the latter regime, reveal [23] a pronounced quasielastic peak (QEP, see Fig. 1) near the Ising-nematic phase transition. The peak height grows proportionally to the thermodynamic nematic susceptibility, and displays a Curie-Weiss behavior as a function of temperature. More interestingly, the peak occurs at a frequency smaller than temperature, and softens as T^α where $\alpha > 1$.

Theoretically, Raman response in the vicinity of an Ising-nematic phase has been studied previously. For example, Ref. [24] showed that a QEP can occur in the presence of impurity scattering. Reference [25] expanded the work by generalizing to a two-orbital model, and notably showed that a depletion of low-frequency Raman spectral weight inside the Ising-nematic phase can be attributed to orbital polarization. However, both have concluded that the QEP frequency scales as the inverse Ising-nematic thermodynamic susceptibility on the disordered side, inconsistent with the experimental findings alluded to earlier. On the other hand, two recent theoretical works [26,27] studied the nematic dynamical response at zero temperature in the presence of electron-electron scattering from critical fluctuations, and predicted an $\omega^{1/3}$ behavior in the low-frequency range, as illustrated by the black dashed line in Fig. 1. However, these studies inevitably missed the QEP feature, which is a finite-temperature phenomenon occurring at $\omega < T$.

In this work, we present a detailed study of the dynamical nematic susceptibility $D_{\text{nem}}(\mathbf{q} \approx 0, \omega)$ at finite temperatures when a two-dimensional electronic system is driven toward an Ising-nematic QCP. Following earlier works [22,28], in a broad finite-temperature regime of experimental interest, the thermally excited electrons are predominantly coherent (coherent electron regime) and the self-energy effects can be neglected. This is the kinetic regime where the electron-electron interaction effects are incorporated into the Landau Fermi liquid parameters and the collision integral. We use a memory matrix approach developed recently [28] to formulate such a kinetic theory. It is an alternative method to the
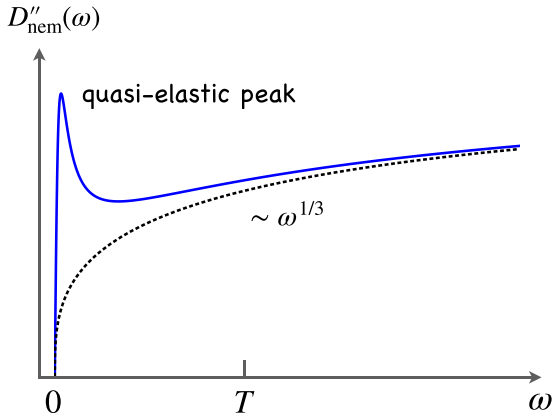
FIG. 1. Schematic plot of the imaginary part of the dynamical nematic susceptibility in the vicinity of an Ising-nematic QCP, featuring a low-frequency quasielastic peak, and $\omega^{1/3}$ dependence at frequencies higher than temperature. The Fermi energy E_F is taken to be much larger than temperature.

Kubo linear response theory, and is excellent at dealing with systems, which exhibit a clear separation of timescales [29].

The main result is sketched in Fig. 1. We argue that the QEP reflects the slow relaxation of an Ising-nematic deformation of the Fermi surface, analogous to the Drude peak in the optical conductivity (which is associated with the slow decay of the current). The frequency of QEP, $\Gamma(T)$, depends on both dynamical and thermodynamic properties. The frequency $\Gamma(T)$ vanishes at the onset of the Ising-nematic order, where an Ising-nematic deformation of the Fermi surface becomes energetically favorable. This is reflected as $\Gamma(T) \propto \chi_{\hat{Q},\hat{Q}}^{-1}$, the inverse Ising-nematic susceptibility. The Ising-nematic deformation of the Fermi surface is relaxed by a combination of impurity scattering and the long wavelength quantum critical fluctuations (with $\omega \ll |v_F \mathbf{q}|$). As we will see, it is natural to define the Ising-nematic dynamical scattering rate as $\tau^{-1}(T) \equiv \Gamma(T)\chi_{\hat{Q},\hat{Q}}(T)$. Whereas in the impurity scattering dominated regime, $\tau^{-1}(T)$ is temperature independent [24,25], in the regime governed by critical fluctuations, it reflects a momentum diffusion process due to small-angle scattering. Finally, at frequencies higher than the temperature, we find that the dynamical susceptibility scales as $\omega^{1/3}$, consistently with earlier work [26].

The content is organized as follows. In Sec. II we briefly introduce the memory matrix approach. In Sec. III we discuss a simple model describing the metallic Ising-nematic quantum critical phenomena, and justify the coherent electron regime at a broad finite temperature window above the quantum critical point. In Sec. IV we perform a calculation of the Raman susceptibility using the memory matrix approach, and make comparisons with recent experimental findings.

II. MEMORY MATRIX APPROACH

We begin with a brief introduction to the memory matrix approach, following the discussions laid out in Refs. [29,30]. It is an exact reformulation of the Kubo linear response theory, and is extremely powerful for studying the low-frequency dynamics for quantum many-body systems where there is a separation of timescales.

We define a dynamical response function for any two Hermitian operators A and B:

$$C_{AB}(t) = T \int_0^\beta d\tau \langle [A(t) - \langle A \rangle][B(i\tau) - \langle B \rangle] \rangle. \quad (1)$$

Here $\beta = 1/T$ is inverse temperature, and $\langle \dots \rangle$ denotes thermal averaging. The time evolution of the Hermitian operators in the Heisenberg picture is given by:

$$A(t - i\tau) = e^{iH(t-i\tau)}A(0)e^{-iH(t-i\tau)}$$
$$\equiv e^{iL(t-i\tau)}A(0), \quad (2)$$

where $L \equiv [H, \cdot]$ is the quantum Liouvillian operator. The dynamical response function is related to the usual definitions of thermodynamic susceptibilities χ_{AB} and retarded response functions $G_{AB}^R(t)$ as follows:

$$\chi_{AB} = \frac{1}{T}C_{AB}(t = 0), \quad (3)$$

$$G_{AB}^R(t) = -\frac{1}{T}\Theta(t)\partial_t C_{AB}(t). \quad (4)$$

It is convenient to rewrite Eq. (1) as the inner product of two vectors:

$$C_{AB}(t) \equiv (A(t)|B) = (A|e^{-iLt}|B), \quad (5)$$

where we have introduced an operator Hilbert space: $\mathcal{H} = \{|A_i), i = 1, \dots\}$. It is straightforward to check that:

$$\mathcal{P} \equiv \frac{1}{T}\sum_{ij}|A_i)\chi_{A_i A_j}^{-1}(A_j|, \quad \mathcal{Q} = I - \mathcal{P} \quad (6)$$

satisfy the definitions of projection operators. $\mathcal{P}|A_i) = |A_i)$ projects onto the subset of operator manifold $\mathcal{H}$, whereas $\mathcal{Q}|A_i) = 0$ projects to the exterior.

The dynamical response function $C_{AB}(t)$ can be interpreted as a matrix element of the superoperator $\hat{C}(t) \equiv e^{-iLt}$. Below we present a reformulation of the superoperator with respect to $\mathcal{H}$. We define a Laplace transform:

$$\hat{C}(z) = \int_0^\infty \mathbf{d}t \, e^{izt}\hat{C}(t) = \frac{i}{z - L}. \quad (7)$$

Here z is defined in the upper half of the complex plane. The expression can be equivalently written as follows:

$$\begin{pmatrix} z - \mathcal{P}L\mathcal{P} & -\mathcal{P}L\mathcal{Q} \\ -\mathcal{Q}L\mathcal{P} & z - \mathcal{Q}L\mathcal{Q} \end{pmatrix} \cdot \begin{pmatrix} \mathcal{P}\hat{C}\mathcal{P} & \mathcal{P}\hat{C}\mathcal{Q} \\ \mathcal{Q}\hat{C}\mathcal{P} & \mathcal{Q}\hat{C}\mathcal{Q} \end{pmatrix} = \begin{pmatrix} i\mathcal{P} & 0 \\ 0 & i\mathcal{Q} \end{pmatrix}. \quad (8)$$

As a result, the matrix elements of $\hat{C}$ projected on to the operator subspace $\mathcal{P}$ is given by:

$$(A_i|\hat{C}(z)|A_j) = T\left[\hat{\chi}\frac{1}{\hat{N} + \hat{M}(z) - iz\hat{\chi}}\hat{\chi}\right]_{ij} \quad (9)$$

where we have defined :

$$\hat{\chi}_{ij} \equiv \frac{1}{T}(A_i|A_j), \quad (10)$$

$$\hat{N}_{ij} \equiv \frac{i}{T}(A_i|L|A_j), \quad (11)$$

$$\hat{M}_{ij}(z) \equiv \frac{i}{T}\left(A_i|L\mathcal{Q}\frac{1}{z - \mathcal{Q}L\mathcal{Q}}\mathcal{Q}L|A_j\right). \quad (12)$$

Equation (9) is the memory matrix formalism for dynamical response functions. So far the expressions are exact, and we have not made assumptions about slow and fast operators. If we treat $L|A_i) \sim O(h)$ as a small parameter (i.e., $\mathcal{P}$ projects onto the slow operator Hilbert space), we have:

$$\hat{M}_{ij}(z) \approx \frac{1}{T}(\dot{A}_i|\hat{C}(z)|\dot{A}_j) + O(h^3), \qquad (13)$$

where $\dot{A}_i \equiv iL|A_i)$. By invoking an assumption about the Hilbert space of slow operators, the dynamical response functions can be calculated with a knowledge of $\{\hat{N}, \hat{\chi}\}$ as well as a perturbative treatment of the memory matrix $\hat{M}(z)$.

III. METALLIC ISING-NEMATIC QUANTUM CRITICAL PHENOMENA

To set the stage we consider a simple boson-fermion model in two dimensions that realizes an Ising-nematic QCP, given by the action:

$$S = \int_0^{1/T} d\tau \left[\sum_{\mathbf{k}\sigma} c_{\mathbf{k}\sigma}^\dagger (\partial_\tau + \varepsilon_{\mathbf{k}}) c_{\mathbf{k}\sigma} + \frac{\lambda}{\sqrt{N}} \sum_{\mathbf{q}} \phi_{\mathbf{q}} \hat{Q}_{-\mathbf{q}} \right]$$
$$+ \int_0^{1/T} d\tau \sum_{\mathbf{q}} \frac{1}{2} [1 + (\mathbf{q}\xi_0)^2] |\phi_{\mathbf{q}}|^2. \qquad (14)$$

Here $c_{\mathbf{k}\sigma}$ annihilates an electron with momentum $\mathbf{k}$ and spin σ. $N = 2$ is the number of spin components (below, we shall generalize the problem to an arbitrary N). For simplicity we consider a parabolic dispersion $\varepsilon_{\mathbf{k}} = |\mathbf{k}|^2/2m - \mu$. The bosonic field $\phi_{\mathbf{q}}$ represents the Ising-nematic fluctuations. The bare nematic propagator is parametrized by the bare correlation length ξ_0. ϕ couples linearly to the fermionic bilinear $\hat{Q}_{-\mathbf{q}} = \sum_{\mathbf{k}\sigma} \varphi_{\mathbf{k},\mathbf{k}+\mathbf{q}} c_{\mathbf{k}\sigma}^\dagger c_{\mathbf{k}+\mathbf{q}\sigma}$, with a coupling strength λ. $\varphi_{\mathbf{k},\mathbf{k}+\mathbf{q}}$ is the Ising-nematic form factor that changes sign under 90-degree in-plane rotation. For simplicity we have used the definition $\varphi_{\mathbf{k},\mathbf{k}'} \equiv (\cos 2\theta_{\mathbf{k}} + \cos 2\theta_{\mathbf{k}'})/2$, where θ is the angle with respect to the k_x axis. Note that λ^2 has unit of energy. We consider an electronically driven nematic QCP due to the coupling term, and set the bare correlation length $\xi_0 = k_F^{-1}$, the Fermi wave number. This is a strong coupling instability $\lambda_c^2 \propto E_F$ analogous to the Stoner instability for ferromagnetism.

The properties of low-energy excitations near the QCP have been studied extensively in the literature, and here we merely quote the results. The long wavelength ϕ fluctuations gain dynamics via Landau damping. In the limit $\omega < |v_F \mathbf{q}| \ll E_F$, it is described by the following propagator:

$$D^{-1}(\mathbf{q}, \omega) \approx r(T) + (\mathbf{q}\xi_0)^2 - i\gamma_{\mathbf{q}}\omega, \qquad (15)$$

where $\gamma_{\mathbf{q}} \propto \gamma \frac{k_F}{q} \cos 2\theta_{\mathbf{q}}$ is the Landau-damping coefficient. A one-loop approximation gives $\gamma = \frac{1}{2\pi} \frac{\lambda^2}{(mv_F)^2}$ (the approximation is formally justified over a finite range of energies in the large N limit). Within the same approximation, the renormalized mass satisfies $r(T) \propto T^2$. However, it has been shown from both field theoretical methods [31] and numerical simulations [32] that $r(T) \propto T$ instead (up to a $\log T$ correction). Throughout this paper, we will assume $r(T) = T$ without a fully self-consistent calculation,

while keeping the one-loop form for the Landau damping coefficient.

The feedback of the critical fluctuations on single-electron properties is captured by a self-energy term: $\Sigma(\mathbf{k}, \omega) \propto \frac{iE_F}{N}|\gamma\omega|^{2/3} \cos^2 2\theta_{\mathbf{k}}$. The self-energy term becomes dominant in the hot regions below an energy scale $\Omega_{\text{NFL}} \propto \lambda^4 E_F^{-1} N^{-3}$, defined as $\Sigma(\Omega_{\text{NFL}}) = \Omega_{\text{NFL}}$. Below this energy scale, the naive large N approximation breaks down [13]. The strong dependence on the fermion flavor number suggests that the non-Fermi liquid scale can be parametrically suppressed by going to the large-N limit [28,33]. This will be assumed to be true throughout this paper, and the physics below the non-Fermi liquid scale is left to future studies.

Although our results are obtained within a simple one-band electronic model described in Eq. (14), the qualitative results on the Raman response due to quantum critical Ising nematic fluctuations, in particular its temperature dependence, remain unchanged for more realistic models. A two-pocket model analysis is carried out in Appendix for comparison.

IV. DYNAMICAL RAMAN RESPONSE IN COHERENT ELECTRON REGIME

In the coherent electron regime ($\Omega_{\text{NFL}} \ll T \ll E_F$) the dynamical properties can be described using a kinetic equation approach, where the effects of critical fluctuations are incorporated into Fermi liquid parameters and the collision integral. In an earlier work [28], we have shown that the kinetic equation can be derived microscopically using the memory matrix formalism discussed in the previous section [29,34], where we treat the electron occupation numbers in the momentum space $\{\hat{n}_{\mathbf{k}\sigma} \equiv c_{\mathbf{k}\sigma}^\dagger c_{\mathbf{k}\sigma}\}$ as the Hilbert space of slow operators.

The dynamical nematic susceptibility is defined via:

$$D_{\text{nem}}(\omega) = i \int_0^\infty dt \, e^{i\omega t} \langle [\hat{Q}(t), \hat{Q}(0)] \rangle, \qquad (16)$$

where $\hat{Q} \equiv \hat{Q}_{\mathbf{q}=0}$. Following Eq. (4), it is related to the dynamical response function Eq. (1) via:

$$D_{\text{nem}}(\omega) = \chi_{\hat{Q},\hat{Q}} + \frac{i\omega}{T} C_{\hat{Q},\hat{Q}}(\omega). \qquad (17)$$

where

$$\frac{C_{\hat{Q},\hat{Q}}(\omega)}{T} = \sum_{\mathbf{k}\sigma;\mathbf{k}'\sigma'} \hat{\chi}_{\hat{Q},\hat{n}_{\mathbf{k}\sigma}} \left[\frac{1}{\hat{M}(\omega) - i\omega\hat{\chi}} \right]_{\hat{n}_{\mathbf{k}\sigma},\hat{n}_{\mathbf{k}'\sigma'}} \hat{\chi}_{\hat{n}_{\mathbf{k}'\sigma'},\hat{Q}}. \qquad (18)$$

The non-frequency-dependent part $\hat{N} = (n_{\mathbf{k}\sigma}|\dot{n}_{\mathbf{k}'\sigma'}) = 0$ due to time reversal and inversion symmetry. The memory matrix $\hat{M}$ is calculated as:

$$\hat{M}_{\hat{n}_{\mathbf{k}\sigma},\hat{n}_{\mathbf{k}'\sigma'}}(\omega) \approx \frac{1}{i\omega} \left[G^R_{\dot{\hat{n}}_{\mathbf{k}\sigma},\dot{\hat{n}}_{\mathbf{k}'\sigma'}}(\omega) - G^R_{\dot{\hat{n}}_{\mathbf{k}\sigma},\dot{\hat{n}}_{\mathbf{k}'\sigma'}}(0) \right], \qquad (19)$$

where we have defined $\dot{\hat{n}}_{\mathbf{k}\sigma} = i[H, \hat{n}_{\mathbf{k}\sigma}]$, and H is the Hamiltonian that corresponds to the action in Eq. (14). In our system, $\dot{\hat{n}}_{\mathbf{k}\sigma}$ is given by:

$$\dot{\hat{n}}_{\mathbf{k}\sigma} = \frac{i\lambda}{\sqrt{N}} \sum_{\mathbf{q}} \phi_{\mathbf{q}} (\varphi_{\mathbf{k},\mathbf{k}-\mathbf{q}} c_{\mathbf{k}\sigma}^\dagger c_{\mathbf{k}-\mathbf{q}\sigma} - \varphi_{\mathbf{k},\mathbf{k}+\mathbf{q}} c_{\mathbf{k}+\mathbf{q}\sigma}^\dagger c_{\mathbf{k}\sigma}). \qquad (20)$$
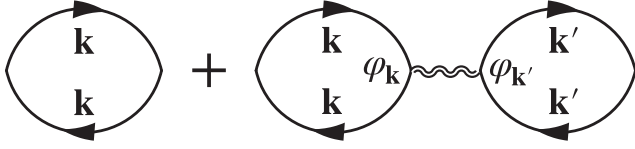
FIG. 2. Feynman diagrams for the thermodynamic susceptibility $\chi_{\hat{n}_{\mathbf{k}}, \hat{n}_{\mathbf{k}'}}$. The double-wiggly line represents the dressed propagator for nematic fluctuations.

The connection of Eq. (17) to a kinetic equation is made by identifying the memory matrix as the linearized collision integral, and the thermodynamic susceptibilities as the Fermi liquid parameters [28].

A. Quasielastic peak

To see that $D_{\text{nem}}(\omega)$ contains a QEP, we treat for simplicity $\hat{Q}$ as the only slow operator (a more rigorous treatment will follow). We arrive at a memory function expression:

$$D_{\text{nem}}(\omega) \approx \frac{M_{\hat{Q},\hat{Q}}(\omega)\chi_{\hat{Q},\hat{Q}}}{M_{\hat{Q},\hat{Q}}(\omega) - i\omega\chi_{\hat{Q},\hat{Q}}}. \quad (21)$$

We write the memory function as $M_{\hat{Q},\hat{Q}}(\omega) = M'(\omega) + iM''(\omega)$. At low frequencies and finite temperatures, the real part can be approximated by its $\omega \to 0$ value, which vanishes as a power law of temperature [28]. The imaginary part is approximately linear in frequency, and renormalizes the strength of the two-particle response. This renormalization is nonsingular and subleading in $1/N$, and hence we neglect it. As a result, $\text{Im} D_{\text{nem}}(\omega)$ contains a low-frequency peak at $\omega \approx M'_{\hat{Q},\hat{Q}}(\omega = 0)/\chi_{\hat{Q},\hat{Q}}$, with a peak height of $\chi_{\hat{Q},\hat{Q}}/2$.

B. Diagrammatic calculation of $\hat{\chi}$ and $\hat{M}$

We perform a diagrammatic calculation of both the memory matrix and the thermodynamic susceptibility to leading order in $1/N$, equivalent to the random phase approximation (RPA). The leading-order Feynman diagrams for the thermodynamic susceptibilities are shown in Fig. 2, where the double-curly line represent the dressed bosonic propagator in Eq. (15), and we have introduced a shorthand notation: $\varphi_{\mathbf{k}} \equiv \varphi_{\mathbf{k},\mathbf{k}}$. We consider the limit when temperature is much smaller than the Fermi energy, and hereby work with the following approximation:

$$\chi_{\hat{n}_{\mathbf{k}\sigma}, \hat{n}_{\mathbf{k}'\sigma'}} \approx \delta_{\mathbf{k}\sigma, \mathbf{k}'\sigma'}\delta(\varepsilon_{\mathbf{k}}) + \frac{\lambda^2}{N}\frac{1}{r(T)}\varphi_{\mathbf{k}}\varphi_{\mathbf{k}'}\delta(\varepsilon_{\mathbf{k}})\delta(\varepsilon_{\mathbf{k}'}). \quad (22)$$

The presence of the δ functions indicates that the main contribution comes from the vicinity of the Fermi surface.

The RPA diagrams for the memory matrix [Eq. (19)] are shown in Figs. 3(a)–3(d). A distinction compared to traditional RPA diagrams for, e.g., compressibility, is that here the memory matrix $\hat{M}_{\hat{n}_{\mathbf{k}\sigma}, \hat{n}_{\mathbf{k}'\sigma'}}$ depends explicitly on the fermionic momenta. This leads to two classes of RPA diagrams shown in Figs. 3(c)–3(d), where the external momentum indices $(\mathbf{k}, \mathbf{k}')$ are colored in red. In Matsubara frequencies, the memory
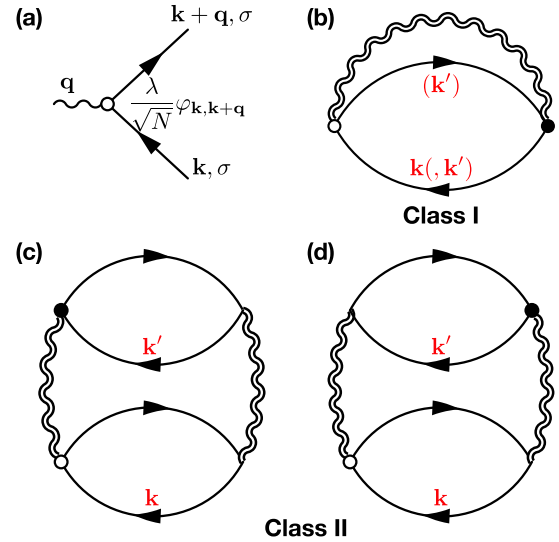

FIG. 3. Feynman diagrams for the memory matrix $\hat{M}_{\hat{n}_{\mathbf{k}\sigma}, \hat{n}_{\mathbf{k}'\sigma'}}$, adapted from Fig. 1 of Ref. [28]. (a) The vertex function for $\dot{n}_{\mathbf{k}\sigma}(\omega)$. The empty (solid) circle at the vertex denotes an incoming (outgoing) frequency ω. (b)–(d) Class I and II Feynman diagrams under random phase approximation. The external momentum indices $(\mathbf{k}, \mathbf{k}')$ are colored red.

matrix is given by:

$$\hat{M}^{(1)}_{\hat{n}_{\mathbf{k}\sigma}, \hat{n}_{\mathbf{k}'\sigma'}}(i\Omega_n) = \delta_{\sigma\sigma'}\frac{\lambda^2 T}{N\Omega_n}\sum_{\mathbf{q},\nu_n} D_{\mathbf{q}, \nu_n + \Omega_n}$$

$$\times \sum_{\zeta = \pm 1} (\delta_{\mathbf{k}-\mathbf{k}',\zeta\mathbf{q}} - \delta_{\mathbf{k},\mathbf{k}'})\varphi^2_{\mathbf{k},\mathbf{k}} R_{\mathbf{k},\mathbf{k}',\zeta\nu_n}, \quad (23)$$

$$\hat{M}^{(2)}_{\hat{n}_{\mathbf{k}\sigma}, \hat{n}_{\mathbf{k}'\sigma'}}(i\Omega_n) = -\frac{\lambda^4 T}{N^2\Omega_n}\sum_{\mathbf{q},\nu_n} D_{\mathbf{q},\nu_n} D_{\mathbf{q},\nu_n + \Omega_n}$$

$$\times \sum_{\zeta\zeta' = \pm 1} \zeta\zeta'\varphi^2_{\mathbf{k},\mathbf{k}+\zeta\mathbf{q}}\varphi^2_{\mathbf{k}',\mathbf{k}'+\zeta'\mathbf{q}} R_{\mathbf{k},\mathbf{k}+\zeta\mathbf{q},\zeta\nu_n}$$

$$\times [R_{\mathbf{k}',\mathbf{k}'+\zeta'\mathbf{q},\zeta'\nu_n} - R_{\mathbf{k}',\mathbf{k}'+\zeta'\mathbf{q},\zeta'(\nu_n + \Omega_n)}]. \quad (24)$$

Here $R_{\mathbf{k},\mathbf{k}',\nu_n}$ is the polarization bubble summed over the fermionic Matsubara frequencies:

$$R_{\mathbf{k},\mathbf{k}',\nu_n} = \frac{n_F(\varepsilon_{\mathbf{k}'}) - n_F(\varepsilon_{\mathbf{k}})}{\varepsilon_{\mathbf{k}} - \varepsilon_{\mathbf{k}'} + i\nu_n}, \quad (25)$$

where $n_F(\varepsilon)$ is the Fermi-Dirac distribution.

A high-frequency expansion [i.e., $\omega\chi \gg \hat{M}(\omega)$] of Eq. (17) shows that the two classes of diagrams correspond to the Maki-Thompson and Density of State [Fig. 3(b)], and Aslamazov-Larkin [Figs. 3(c)–3(d)] diagrams. In the low-frequency limit, Eq. (17) is equivalent to the quantum Boltzmann equation described in the Kadanoff-Baym-Keldysh framework. Below we consider two limiting cases where either $\omega \ll T \ll E_F$ (quasielastic limit) or $T \ll \omega \ll E_F$ (intermediate frequencies).

C. Quasielastic limit

The memory matrix in the quasielastic limit ($\omega \to 0$) describes the scattering processes in the vicinity of the Fermi surface. It has been worked out in Ref. [28], and here we merely quote the results:

$$\hat{M}^{(1)}_{\hat{n}_{\mathbf{k}\sigma},\hat{n}_{\mathbf{k'}\sigma'}} \approx \delta_{\sigma\sigma'} \frac{2\pi\lambda^2}{N} \sum_{\mathbf{q}} V_{\mathbf{q}}(T) \varphi^2_{\mathbf{k},\mathbf{k+q}}$$

$$\times (\delta_{\mathbf{k},\mathbf{k'}} - \delta_{\mathbf{k'-k},\mathbf{q}}) \delta(\varepsilon_{\mathbf{k}}) \delta(\varepsilon_{\mathbf{k+q}}), \qquad (26)$$

$$\hat{M}^{(2)}_{\hat{n}_{\mathbf{k}\sigma},\hat{n}_{\mathbf{k'}\sigma'}} \approx -\frac{2\pi^2\lambda^4}{N^2} \sum_{\mathbf{q}} \frac{V_{\mathbf{q}}(T)}{\gamma_{\mathbf{q}}} \varphi^2_{\mathbf{k},\mathbf{k+q}} \delta(\varepsilon_{\mathbf{k}}) \delta(\varepsilon_{\mathbf{k+q}})$$

$$\times \sum_{\zeta'=\pm 1} \zeta' \varphi^2_{\mathbf{k'},\mathbf{k'}+\zeta'\mathbf{q}} \delta(\varepsilon_{\mathbf{k'}}) \delta(\varepsilon_{\mathbf{k'}+\zeta'\mathbf{q}}), \qquad (27)$$

where

$$V_{\mathbf{q}}(T) = \int_{-\infty}^{\infty} \frac{d\omega}{\pi} \omega D''(\mathbf{q}, \omega) \left(-\frac{\partial n_B(\omega)}{\partial \omega} \right). \qquad (28)$$

It is convenient to work in the angular momentum basis $\hat{M}_{n\sigma,m\sigma'} = \sum_{\mathbf{kk'}} e^{-i(m\theta_{\mathbf{k}}-n\theta_{\mathbf{k'}})} \hat{M}_{\hat{n}_{\mathbf{k}\sigma},\hat{n}_{\mathbf{k'}\sigma'}}$, where the memory matrix has a simple form:

$$\hat{M}_{n\sigma,m\sigma'} \approx \frac{\pi\lambda^2}{N} \sum_{\mathbf{kk'}} f^*_{n,\mathbf{kk'}} f_{m,\mathbf{kk'}} V_{\mathbf{k-k'}}(T) \varphi^2_{\mathbf{k},\mathbf{k'}} \delta(\varepsilon_{\mathbf{k}}) \delta(\varepsilon_{\mathbf{k'}})$$

$$\times \left[\delta_{\sigma\sigma'} - \frac{1}{N} \frac{1-(-1)^n}{2} \frac{1-(-1)^m}{2} \right], \qquad (29)$$

where $f_{m,\mathbf{kk'}} = e^{im\theta_{\mathbf{k}}} - e^{im\theta_{\mathbf{k'}}}$.

Since $\varphi_{\mathbf{k},\mathbf{k'}}$ has even parity, $\hat{M}_{n\sigma,m\sigma'}$ hybridizes angular harmonics (n, m) of the same parity. For a given pair of (n, m), $\hat{M}_{n\sigma,m\sigma'}$ has a simple matrix structure in the spin (flavor) basis. For even-parity modes such as $\hat{Q}$, $\hat{M}_{n\sigma,m\sigma'} \propto \delta_{\sigma,\sigma'}$ is diagonal in the spin (flavor) space, and nonzero corresponding to a finite decay lifetime. However, for odd-parity modes, the diagonal matrix elements are $1 - \frac{1}{N}$, and the other entries are $-\frac{1}{N}$. This leads to one zero mode with eigenvector $\frac{1}{\sqrt{N}}(1, 1, \dots)$. Hence, odd parity deformations of the Fermi surface are long lived. This dichotomy of even-odd parity modes is unique to two-dimensional electronic systems, and has been discussed previously in Ref. [35,36].

In the angular harmonics basis, Eq. (17) has a simpler expression, given by:

$$D_{\text{nem}}(\omega) \approx \chi_{\hat{Q},\hat{Q}} + i\omega \chi^2_{\hat{Q},\hat{Q}} \left[\frac{1}{\hat{M}(\omega) - i\omega\hat{\chi}} \right]_{\hat{Q},\hat{Q}}. \qquad (30)$$

This simplification is due to the fact that $\hat{\chi}_{n,m} \propto \delta_{n,m}$ according to Eq. (22). Note that there is a crucial difference compared to Eq. (21). Here the matrix in the square brackets is first inverted before taking the overlap with the Ising-nematic form factor. Due to the hybridization of different angular harmonics [see Eq. (29)], two expressions may give qualitatively different results.

We first present a qualitative analysis for the temperature dependence of the QEP frequency. Since critical fluctuations give rise to small-angle scattering, we expect that the decay of an Ising-nematic deformation of the Fermi surface to be governed by momentum diffusion, which leads to a decay rate
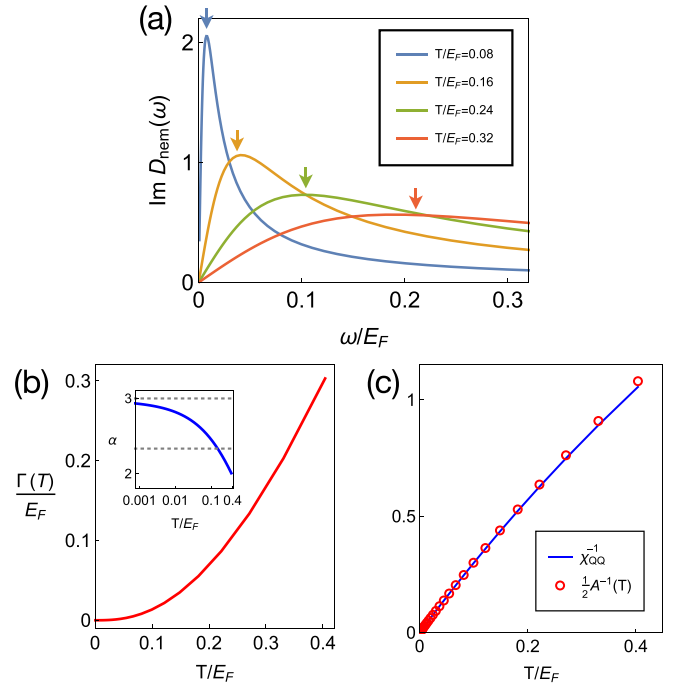

FIG. 4. (a) Imaginary part of the dynamical nematic susceptibility showing a quasielastic peak feature for various temperatures. (b) QEP peak frequency $\Gamma(T)$ as a function of temperature. Inset is the log-derivative plot $\alpha \equiv d\ln\Gamma/d\ln T$ showing the temperature variation of the power-law exponent. The dashed lines correspond to $T^2\chi^{-1}$ (Fermi liquid behavior) and $T^{4/3}\chi^{-1}$. (c) Inverse of the QEP peak height $A(T)$ (red circle) compared the thermodynamic susceptibility (blue solid line).

$\tau^{-1} \propto (q_0/k_F)^2 \tau_0^{-1}$, where τ_0^{-1} is the single-particle scattering rate, and q_0 is the characteristic momentum transfer. $q_0 \sim T^{1/3}$ and $\tau_0^{-1} \sim T^{2/3}$ following quantum critical scaling. As a result, the QEP frequency should scale as $\tau^{-1}\chi_{\hat{Q},\hat{Q}}^{-1} \propto T^{7/3}$ near the QCP.

In Fig. 4 we present a numerical solution for the low-frequency Raman response for a clean system, replacing the memory matrix by its $\omega \to 0$ limit. We choose $\lambda^2 = 2\pi N E_F$ (RPA instability) and $N = 2$. Figure 4(a) shows the response for various temperatures. The spectral response clearly shows the development of a low-frequency peak as temperature is lowered toward the QCP. The temperature dependence of the peak height and peak frequency are presented in Figs. 4(b) and 4(c), respectively. As expected, the peak height tracks the thermodynamic susceptibility, while the peak frequency softens toward the QCP. However, the temperature dependence of the peak frequency cannot be fitted to a simple power law governed by momentum diffusion. The log-derivative plot [Fig. 4(b) inset] shows a smooth variation of the exponent as temperature is lowered, saturating to T^3 at low temperatures. Since the QEP is a weighted superposition of eigenmodes of $[\hat{M}(\omega) - i\omega\hat{\chi}]^{-1}$, there is not the notion of a single scattering time as discussed in the naive quantum critical scaling previously. It is nonetheless useful to define $\tau^{-1} \equiv \Gamma(T)\chi_{\hat{Q},\hat{Q}}$ to separate the dynamic component of the QEP. Figure 4 then implies that $\tau^{-1} \propto T^2$ as $T \to 0$—analogous to that of a Fermi liquid, despite being at the QCP.
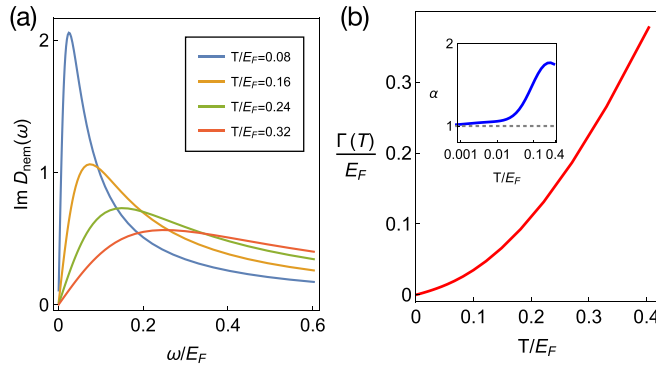
FIG. 5. (a) Imaginary part of the dynamical nematic susceptibility in the presence of impurity scattering ($g_{\mathrm{imp}} = 0.1E_F$). (b) QEP peak frequency $\Gamma(T)$ as a function of temperature. Inset is the log-derivative plot showing the temperature variation of the power-law exponent α.
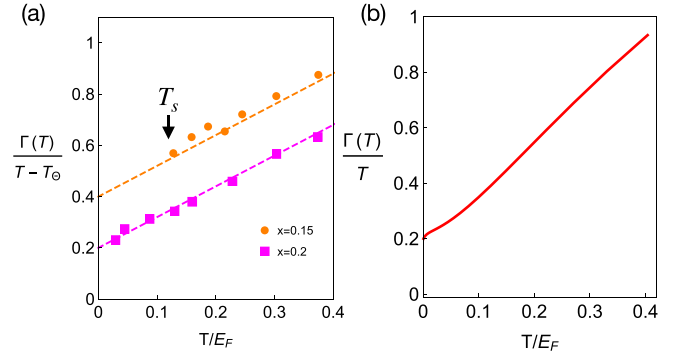

FIG. 6. (a) Quasielastic peak frequency for FeSe$_{1-x}$S$_x$ at dopings $x = 0.15$ (orange) and $x = 0.2$ (magenta), extracted from Ref. [23]. The extrapolated Curie-Weiss temperature is zero at $x = 0.15$, and negative at $x = 0.2$. E_F is taken to be 30 meV. The dashed lines are linear fits using $a + 1.2T/E_F$, with $a = 0.2$ and 0.4, respectively. (b) A replot of Fig. 5(b) with the y axis being $\Gamma(T)/T$.

The apparent violation of the naive quantum critical scaling at all temperatures can be understood as follows. At high temperatures, $V_{\mathbf{q}}(T) \propto \frac{T\gamma_{\mathbf{q}}}{r(T)+\mathbf{q}^2}$ from Eq. (28). The typical momentum transfer $q_0 \sim k_F \ll r(T)$. As a result, $V_{\mathbf{q}}(T) \propto \frac{T\gamma_{q_0}}{r(T)} \sim$ const, leading to a constant lifetime. At low temperatures, the typical momentum transfer $q_0 \sim k_F(\gamma T)^{1/3}$ is small. Furthermore, the Fermi surface is divided into four weakly connected patches by the Ising-nematic cold spots, where the form factors vanish by symmetry. Scattering across the cold spots is the bottleneck for global equilibration. Evaluating the memory matrix [Eq. (29)] near the cold spots, we get $M \propto \int_0^{q_0} d^2q\, q^4 V_q \sim T^2$. Compared to rate of momentum diffusion, there is an additional factor of q_0^2 due to the form factor.

Next, we consider how impurity scattering affects the properties of the QEP. For simplicity we assume the impurity scattering only contributes to the memory matrix $M(T) = M_{\mathrm{nem}}(T) + M_{\mathrm{imp}}(T)$ but does not modify the thermodynamic properties. Now, the cold spots are no longer a bottleneck for relaxation, and as a result $\Gamma(T) \propto [\tau_{\mathrm{imp}}^{-1} + \tau_{\mathrm{nem}}^{-1}(T)]\chi_{\hat{Q},\hat{Q}}^{-1}$. At low temperatures impurity scattering is dominant, leading to $\Gamma(T) \propto T$ coming from the thermodynamic susceptibility. This is the behavior discussed in Refs. [24,25]. At higher temperatures, nematic fluctuations are more important, leading to a stronger temperature dependence. This behavior is illustrated in Fig. 5.

D. Intermediate frequencies

We proceed to study the limit where the external frequency is much larger than temperature. Here, the memory matrix in Eq. (17) is always smaller than $\omega\chi_{\hat{Q},\hat{Q}}$. As a result, the approximate memory function expression in Eq. (21) holds. It is straightforward to show that $M_{\hat{Q},\hat{Q}}(\omega) \propto \omega^{4/3}$ governed by momentum diffusion. The imaginary part of the Raman response is then given by:

$$\mathrm{Im}D_{\mathrm{nem}}(\omega) \approx \frac{M_{\hat{Q},\hat{Q}}(\omega)}{\omega} \propto \omega^{1/3}. \tag{31}$$

This behavior has also been obtained in earlier works using perturbative diagrammatic techniques at zero temperature [26,27].

V. SUMMARY AND OUTLOOK

So far we have neglected the effects of acoustic phonons. As argued in Ref. [20], the nematoelastic coupling shifts the position of the Ising-nematic phase transition temperature. Experimentally this is reflected in the difference between the extrapolated Curie-Weiss temperature T_Θ and measured transition temperature T_s [23]. Moreover, the coupling leads to directional criticality at the QCP, where the correlation length is divergent only along the diagonal directions of the Brillouin zone. As discussed in Refs. [19,20,37,38], this can also lead to a breakdown of quantum critical scaling, and recover Fermi liquid behavior at low temperatures.

We proceed to compare our results to Raman scattering experiments performed on FeSe$_{1-x}$S$_x$ [23], where a putative Ising-nematic QCP occurs at $x \approx 0.15$. In Fig. 6(a) we plot $\Gamma(T)/(T - T_\Theta)$ as a function of T/E_F for $x = 0.15, 0.2$, extracted from the experiments. As discussed earlier, this quantity represents the dynamical contributions to the QEP. Above $T_s(x)$, the data can be fitted using a functional form $a + bT$, suggesting that the near-critical Ising-nematic fluctuations give rise to a linear-in-T scattering rate. This behavior is qualitatively captured from our calculation shown in Fig. 6(b), a replot of Fig. 5(b), without fine tuning of parameters except the strength of impurity scattering.

In summary, using a memory matrix approach, we studied the dynamical nematic susceptibility for a two-dimensional electronic system near an Ising-nematic quantum critical point. Our results are qualitatively consistent with the Raman scattering results for FeSe$_{1-x}$S$_x$. Interestingly, we find it useful to separate the dynamical and thermodynamic contributions to the quasielastic peak frequency $\Gamma(T) \propto \tau^{-1}\chi_{\hat{Q},\hat{Q}}^{-1}$. As a result, a dynamical scattering rate τ^{-1} can be extracted directly from experimental data via the product of the peak frequency with the thermodynamic susceptibility.
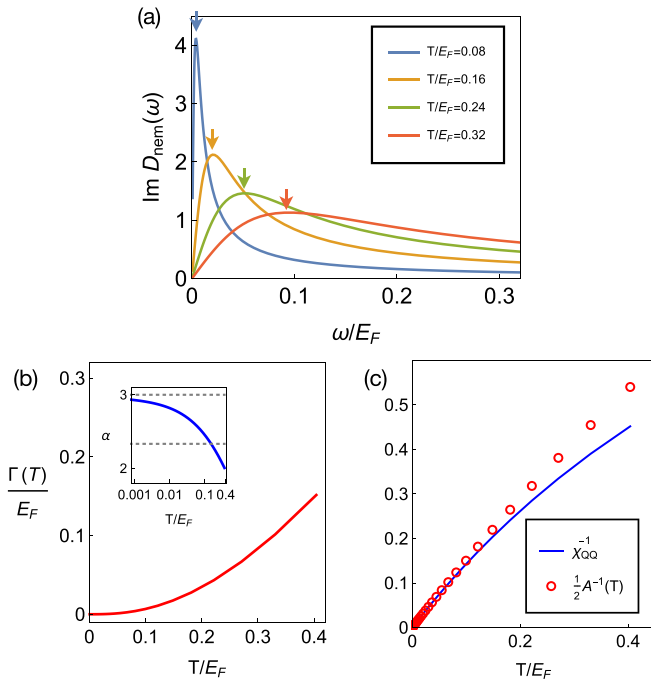
FIG. 7. Raman response for a two-pocket electronic model in the clean limit. Compared to Fig. 4, here the quasielastic peak frequency is reduced by a factor of 2 due to fermion band doubling, but the power-law temperature dependence remains unchanged, showing a universal behavior independent on band structure details.

APPENDIX: MEMORY MATRIX CALCULATION OF RAMAN RESPONSE IN A TWO-POCKET MODEL

We begin by noting that under RPA, the memory matrix: $M \sim O(N^0)$, and the thermodynamic susceptibility $\chi \sim O(N)$, and as a result, the quasielastic peak frequency: $\Gamma(T) \sim O(1/N)$.

In the regime governed by Ising-nematic quantum critical fluctuations, the qualitative features of the low-frequency Raman response are insensitive to the microscopic band parameters except for the presence/absence of Ising-nematic cold spots on the Fermi surface. To illustrate this, here we present an analysis of a two Fermi-pocket model, with a circular hole pocket centered at the Γ point and a circular electron pocket centered at the M point of the Brillouin zone. The dispersions are chosen as $\varepsilon_{h,\mathbf{k}} = \frac{k^2}{2m} - \mu$ and $\varepsilon_{e,\mathbf{k}+\mathbf{Q}} = -\varepsilon_{h,\mathbf{k}}$, where $\mathbf{Q} = (\pi/a, \pi/a)$. We choose $m = 1$, $k_F = 1$. The Ising-nematic QCP is achieved at $\lambda^2 = 4\pi N E_F$ at the RPA level, where $N = 4$ corresponding to two pockets and two spin species. The Raman response in the clean limit is illustrated in Figure. 7. A comparison with Fig. 4 of the main text shows that while the quasielastic peak frequency $\Gamma(T)$ is suppressed, its temperature-dependent power-law exponent [inset to Fig. 4(b)] remains qualitatively unchanged.

[1] R. Daou, J. Chang, D. LeBoeuf, O. Cyr-Choinière, F. Laliberté, N. Doiron-Leyraud, B. J. Ramshaw, R. Liang, D. A. Bonn, W. N. Hardy *et al.*, Nature (London) **463**, 519 (2010).

[2] J.-H. Chu, J. G. Analytis, K. De Greve, P. L. McMahon, Z. Islam, Y. Yamamoto, and I. R. Fisher, Science **329**, 824 (2010).

[3] Y. Kohsaka, C. Taylor, K. Fujita, A. Schmidt, C. Lupien, T. Hanaguri, M. Azuma, M. Takano, H. Eisaki, H. Takagi, S. Uchida, and J. Davis, Science **315**, 1380 (2007).

[4] A. E. Böhmer and C. Meingast, C. R. Phys. **17**, 90 (2016).

[5] A. I. Coldea and M. D. Watson, Annu. Rev. Condens. Matter Phys. **9**, 125 (2018).

[6] P. Reiss, D. Graf, A. A. Haghighirad, W. Knafo, L. Drigo, M. Bristow, A. J. Schofield, and A. I. Coldea, Nat. Phys. **16**, 89 (2020).

[7] S. Hosoi, K. Matsuura, K. Ishida, H. Wang, Y. Mizukami, T. Watashige, S. Kasahara, Y. Matsuda, and T. Shibauchi, Proc. Natl. Acad. Sci. USA **113**, 8139 (2016).

[8] T. Urata, Y. Tanabe, K. K. Huynh, H. Oguro, K. Watanabe, and K. Tanigaki, arXiv:1608.01044.

[9] P. Reiss, M. D. Watson, T. K. Kim, A. A. Haghighirad, D. N. Woodruff, M. Bruma, S. J. Clarke, and A. I. Coldea, Phys. Rev. B **96**, 121103(R) (2017).

[10] V. Oganesyan, S. A. Kivelson, and E. Fradkin, Phys. Rev. B **64**, 195109 (2001).

[11] W. Metzner, D. Rohe, and S. Andergassen, Phys. Rev. Lett. **91**, 066402 (2003).

[12] M. J. Lawler, D. G. Barci, V. Fernández, E. Fradkin, and L. Oxman, Phys. Rev. B **73**, 085101 (2006).

[13] S.-S. Lee, Phys. Rev. B **80**, 165102 (2009).

[14] E. Fradkin, S. A. Kivelson, M. J. Lawler, J. P. Eisenstein, and A. P. Mackenzie, Annu. Rev. Condens. Matter Phys. **1**, 153 (2010).

[15] M. A. Metlitski and S. Sachdev, Phys. Rev. B **82**, 075127 (2010).

[16] D. F. Mross, J. McGreevy, H. Liu, and T. Senthil, Phys. Rev. B **82**, 045121 (2010).

[17] R. M. Fernandes, A. V. Chubukov, and J. Schmalian, Nature Phys. **10**, 97 (2014).

[18] T. Holder and W. Metzner, Phys. Rev. B **92**, 041112(R) (2015).

[19] U. Karahasanovic and J. Schmalian, Phys. Rev. B **93**, 064520 (2016).

[20] I. Paul and M. Garst, Phys. Rev. Lett. **118**, 227601 (2017).

[21] S. Lederer, Y. Schattner, E. Berg, and S. A. Kivelson, Phys. Rev. Lett. **114**, 097001 (2015).

[22] E. Berg, S. Lederer, Y. Schattner, and S. Trebst, Annu. Rev. Condens. Matter Phys. **10**, 63 (2019).

[23] W. Zhang, S. Wu, S. Kasahara, T. Shibauchi, Y. Matsuda, and G. Blumberg, Proc. Natl. Acad. Sci. USA **118**, 20 (2021).

[24] Y. Gallais and I. Paul, C. R. Phys. **17**, 113 (2016).

[25] M. Udina, M. Grilli, L. Benfatto, and A. V. Chubukov, Phys. Rev. Lett. **124**, 197602 (2020).

[26] A. Klein, S. Lederer, D. Chowdhury, E. Berg, and A. Chubukov, Phys. Rev. B **98**, 041101(R) (2018).

[27] A. Klein, S. Lederer, D. Chowdhury, E. Berg, and A. Chubukov, Phys. Rev. B **97**, 155115 (2018).

[28] X. Wang and E. Berg, Phys. Rev. B **99**, 235136 (2019).

[29] S. Hartnoll, A. Lucas, and S. Sachdev, *Holographic Quantum matter* (The MIT Press, Cambridge, 2018).

[30] C. G. Wang, Z. Li, J. Yang, L. Y. Xing, G. Y. Dai, X. C. Wang, C. Q. Jin, R. Zhou, and G.-q. Zheng, Phys. Rev. Lett. **121**, 167004 (2018).

[31] S. A. Hartnoll, R. Mahajan, M. Punk, and S. Sachdev, Phys. Rev. B **89**, 155130 (2014).

[32] Y. Schattner, S. Lederer, S. A. Kivelson, and E. Berg, Phys. Rev. X **6**, 031028 (2016).

[33] M. A. Metlitski, D. F. Mross, S. Sachdev, and T. Senthil, Phys. Rev. B **91**, 115111 (2015).

[34] D. Forster, *Hydrodynamic Fluctuations, Broken Symmetry, and Correlation Functions* (CRC Press, Boca Raton, 2018).

[35] D. L. Maslov, V. I. Yudson, and A. V. Chubukov, Phys. Rev. Lett. **106**, 106403 (2011).

[36] P. J. Ledwith, H. Guo, A. V. Shytov, and L. Levitov, Phys. Rev. Lett. **123**, 116601 (2019).

[37] V. S. de Carvalho and R. M. Fernandes, Phys. Rev. B **100**, 115103 (2019).

[38] L. E. Vieira, V. S. de Carvalho, and H. Freire, Ann. Phys. (NY) **419**, 168230 (2020).